The effect of laser assisted tape placement processing conditions on microstructural evolution, residual stress and interlaminar shear strength of carbon fibre/PEEK laminates

Ma, Hong; Bandaru, Aswani Kumar; Weaver, Paul M.

Published in:
Composites Part B: Engineering

Link to article, DOI:
10.1016/j.compositesb.2024.111293

Publication date:
2024

Document Version
Publisher's PDF, also known as Version of record

Composites Part B 274 (2024) 111293

Contents lists available at ScienceDirect

Composites Part B

journal homepage: www.elsevier.com/locate/compositesb

The effect of laser assisted tape placement processing conditions on microstructural evolution, residual stress and interlaminar shear strength of carbon fibre/PEEK laminates

Hong Ma [a,b], Aswani Kumar Bandaru [a,*], Paul M. Weaver [a]

[a] Bernal Institute, School of Engineering, University of Limerick, V94 T9PX, Ireland
[b] Department of Wind and Energy Systems, Technical University of Denmark, Roskilde, DK4000, Denmark

ARTICLE INFO

Handling Editor: Prof. Ole Thomsen

Keywords:
Laser assisted tape placement
Crystallisation
Fibre/matrix crystalline interphase
Thermo-mechanical coupled simulation
Interlaminar shear strength
Fracture behaviour

ABSTRACT

In the present study, both experiments and thermo-mechanical coupled simulations were conducted to characterise the diverse crystallisation behaviours and the processing parameter-microstructure-mechanical property relationships occurring in laser-assisted tape placement (LATP) manufacturing of carbon fibre (CF)/Polyetheretherketone (PEEK) laminates. Specifically, at various processing temperatures (350 °C or 400 °C), increasing the compaction pressure from 2 to 4 bar causes distinct defect distribution behaviours. However, variations in processing parameters show minimal effect on the morphology and size of crystallised spherulites, which were consistently around 2–3 μm in size, resulting in a final crystallinity of manufactured laminates within 30%–35%. It was found that the cold crystallisation processes occurring in PEEK during LATP play an important role in determining the final degree of crystallinity. Experimental measurements and simulations indicate that changes in processing parameters have a negligible effect on residual stress levels, especially regarding interlaminar residual stresses. A processing temperature of 400 °C was found to generate a diffuse, yet coherent, interphase spanning the fibre/matrix interface with a thickness approximately 70 nm. In contrast, at a processing temperature of 350 °C, a distinct, incoherent interface was confirmed between fibre and matrix. The formation of the interphase, coupled with fewer defects, leading to a relatively high interlaminar shear strength (78 MPa) of manufactured laminates under appropriate processing conditions. Therefore, it is suggested that regulating the degree of cold crystallisation in polymer matrices while ensuring a strong fibre/matrix interfacial bond by the optimisation of processing temperature, will enable the tailoring of microstructure and design of composites to meet specific strength property requirements.

1. Introduction

Automated tape placement (ATP) offers a rapid approach for the additive manufacture of high-performance carbon fibre reinforced thermoplastic polymer composite materials with significant potential applications in aerospace and automotive industries [1]. Various heating sources have been employed, including hot-gas torch, laser, and heat lamp [2]. Among these alternatives, laser offers distinct advantages, including high thermal energy efficiency and high-speed processing, making it a preferred choice for ATP, which is often referred to as laser assisted tape placement (LATP). During ATP processing, both surfaces of the incoming composite tape and the substrate are heated. Under the subsequent application of a pressure imposed by a compaction roller on the hot surfaces, an intimate contact between the hot composite tape and the substrate occurs, and in so doing, realises consolidation of the composite tapes [2,3], as shown in Fig. 1a and b. Because of the instant high heating and cooling rate characteristics, the microstructure, including crystallisation in semi-crystalline matrices and defects, the development of residual stresses and possible matrix degradation during manufacture, are different to those observed in similar composite laminates prepared by autoclave/hot press where a slow heating/cooling rate and a long dwell time are commonly used [4]. These differences necessitate the in-depth analysis of the effects of processing parameters on the interactions between composite microstructure, residual stress development and the resulting material properties, for optimising the manufacturing process.

* Corresponding author.
E-mail address: aswani.bandaru@ul.ie (A.K. Bandaru).

https://doi.org/10.1016/j.compositesb.2024.111293
Received 13 December 2023; Received in revised form 19 January 2024; Accepted 5 February 2024
Available online 6 February 2024

The most prevalent defect type developed during ATP are voids, the presence of which significantly degrades strength properties, particularly the bonding quality between different plies (layers). The suppression of voids largely depends on the degree of intimate contact between plies at high temperatures. Samak et al. [5] reported that voids could be reduced by a higher pressure arising from an improved degree of contact of the viscous thermoplastic matrix, while Tierney and Gillespie [6] highlighted the non-uniformity of voids inside laminates prepared by ATP by considering the de-consolidation mechanisms and heat sink effects at the top and bottom surfaces, respectively in comparison with central areas (Fig. 1b and c). The high cooling and heating rates also resulted in a non-equilibrium microstructure for the semi-crystalline matrix which hinders development of the crystalline phase, i.e., spherulites, to nucleate and grow, overall leading to relatively low-level crystallinity compared to laminates prepared by either autoclave or hot press [2,3]. Nevertheless, by altering the deposition velocity, the crystallinity levels could change significantly. By summarising the relevant data from literature, Donough et al. [7] found that the crystallinity of carbon fibre (CF)/polyether ether ketone (PEEK) composites could be able to decrease from around 30% to 10% when the deposition velocity increased from 20 mm/s to 1000 mm/s. Kotzur et al. [8] found that due to different cooling conditions for CF/polyphenylene sulphide (PPS) laminates during ATP, different crystalline structures can be obtained at various locations within the laminate, as illustrated in Fig. 1c. Apart from microstructure, the residual stress development during manufacturing and the final residual stress field should also be addressed, because in ATP, especially for LATP, heat is localised to a localised region (Fig. 1b), causing large thermal gradients, which could create severe levels of residual stress. By adjusting tape tension, Lü et al. [9] experimentally revealed that residual stress levels can be changed in both CF/PEEK and glass fibre–polypropylene (G–PP) laminates. These observations show that more detailed study is required to better understand the variation in processing parameters on the microstructure and residual stress levels and distribution in laminates manufactured by ATP.

From the discussion of the literature, it can be deduced, since ATP is a coupled thermomechanical process, that heat transfer as well as residual stress development are significant factors in influencing the microstructure and magnitudes and mechanical performances of the resulting laminates. Therefore, numerical models combining heat transfer mechanisms and residual stress evolution processes are important tools in establishing the relationship between processing parameters and mechanical performance, with the potential to better optimise the ATP process. A number of studies paid considerable attention to developing an appropriate heat transfer model. Based on the specific heat source, different approaches, including the ray-tracing method (thermal-optical model) for laser [11] and modification of convection load for hot gas [12], have been successfully adopted to address the interaction of heat source with the composite tape. By employing an optical-thermal model, the effects of roller indentation [13], consolidation velocity [14], type of material [15] and laser tilt angle [11], on the temperature distribution during LATP were investigated, which provided useful information on analysing the development of matrix microstructure and for the optimisation of processing parameters. A residual stress analysis model was developed by Sonmez et al. [16] where they found that the processing parameters affected residual stresses via their influence on the temperature distribution. Unfortunately, a coupled thermomechanical model, which provides a more straightforward approach to simultaneously analyse stress and temperature development, has still not been widely reported. Recently, a thermomechanical model was proposed by Heathman et al. [17], from which the variation of temperature as well as the pressure before and after roller compaction was obtained, nevertheless, the study employed an over-simplified heat flux distribution model and a temperature-dependent elastic constitutive model. A material model that considers the viscoelastic behaviour of polymer matrices, coupled with the optical-thermal model, could offer a more realistic representation of the response of composite tape, especially considering the relatively high processing temperatures used during manufacture.

Taking into account the aforementioned considerations, this present study conducts a detailed examination of the microstructure and mechanical properties of CF/PEEK composites fabricated under varying LATP conditions. The effect of LATP parameters, i.e., compaction pressure and temperature on residual stresses is also addressed. Additionally, a coupled thermomechanical finite element model for ATP, drawing upon thermal-optical and viscoelastic models, to characterise thermal history and stress development, is developed. The crystallinity and interfacial microstructure between the fibre and matrix are discussed in detail linked to the processing temperature from the model. Building upon these findings, the interplay between ATP parameters, microstructure, and mechanical properties is discussed, with the aim of offering insights into optimising the LATP process for the manufacture of high-performance CF/PEEK laminates.

2. Materials and methods

2.1. Materials and specimen preparation

The thermoplastic composite tape used in the present study is a commercial aerospace grade CF (Hexcel IM7)/PEEK (PEEK-150) prepreg material with a fibre volume fraction of 60% supplied by Suprem (Switzerland). The tape is 12 mm wide and 0.14 mm thick. A tape placement head (AFPT, GmbH) attached to a robot arm was used to perform LATP on a drum mandrel (diameter: 75 mm), as shown in Fig. 2.

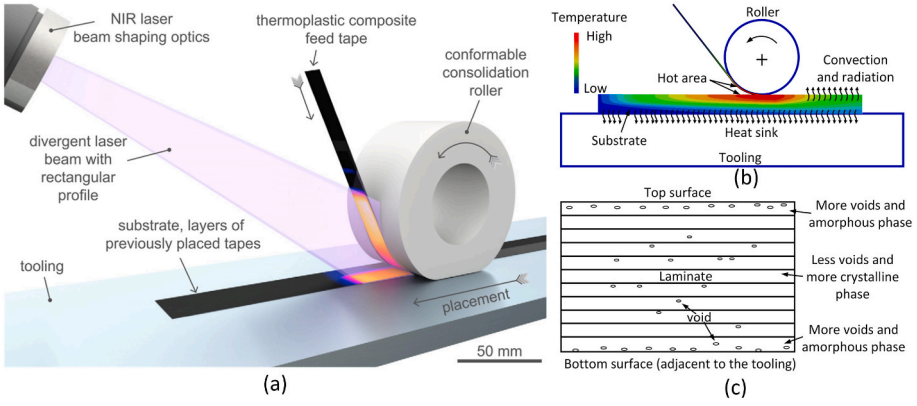

Fig. 1. (a) Illustration of LATP [10], (b) temperature distribution on the incoming tape and substrate during ATP and (c) non-uniform distribution of voids and matrix morphology.

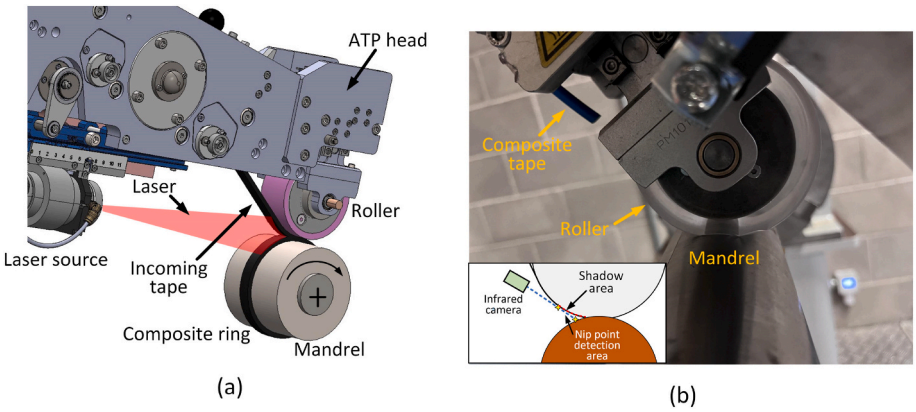

Fig. 2. (a) Schematic illustration and (b) snapshot of LATP process used in the present study.

The head, illustrated in Fig. 2a, consists of an optical lens connected to a diode-laser, a tape feed system, a silicone compaction roller with a diameter of 40 mm and an infrared camera for temperature monitoring. The laser power is controlled by the second highest temperature in the nip point region required by the IR camera. It is known that there exists a shadow area prior to nip point which leads to rapid temperature reduction in that region, as illustrated by the bottom inset in Fig. 2b. As this study accounts for the temperature drop in the shadow area, the controlled highest temperature is referred to as the processing temperature, as opposed to the nip point temperature, which is not the hottest point but is the most commonly referred to position in the literature, when discussing maximum temperatures. During manufacture, the incoming tape is continuously heated by the laser and wound onto the rotating mandrel. In this study, various processing temperatures and compaction pressures were used, as listed in Table 1. The manufactured laminates were identified according to the parameters used (Table 1). Because residual stress is of interest, 70 layers of composite tape were consolidated to manufacture a full composite ring so as to perform residual stress measurement by the central hole drilling method [18], which is introduced later in Section 2.3. The average laser power used to reach the target processing temperature, is also summarised in Table 1. Note that the processing temperature adopted in the present study does not lead to discernible matrix degradation [19]. Therefore, matrix degradation and its effects on the crystallisation process are not discussed further.

2.2. Mechanical and morphological characterisation

After manufacture, wrinkles were identified on both sides of the composite ring (see section 3.1). So before mechanical and morphological characterisation, two sides of the composite ring were machined until a flat edge was obtained. The interlaminar shear strength (ILSS) was measured using a short beam shear (SBS) test in a three-point bending configuration. A minimum of three curved samples per specimen were cut from the composite ring based on the geometry required by ASTM D2344 [20].The ILSS test was performed at a constant displacement rate of 1 mm/min with a universal testing machine (H25K-S, Tinius Olsen). The maximum load was utilised to calculate the ILSS based on the following relation [21]:

Table 1
Process parameter and corresponding specimen identity.

Specimen identity (label)	Temperature (°C)	Pressure (bar)	Speed (mm/min)	Power (W)
350–2	350	2	4	438.4
350–4	350	4		457.1
400–2	400	2		519.8
400–4	400	4		541.4

$$\tau = \frac{3}{4} \times \frac{P}{b \times w} \tag{1}$$

where P is the maximum load, b and w are the thickness and width of the specimens, respectively.

Before microscopic analysis by optical microscopy (OM, Axio Imager, Zeiss) was undertaken, the cross-sections of untested specimens were ground and polished according to usual metallographic procedures. To further reveal the morphology of the crystalline phase, the polished samples were etched by a solution consisting of potassium permanganate, sulphuric acid, orthophosphoric acid and distilled water, followed by scanning electron microscopy (SEM, SU70, Hitachi). Both cross-sectional and fracture surfaces from the post-mortem ILSS test composite specimens were investigated by OM and SEM respectively to facilitate the identification of the fracture behaviour in the ILSS test. To reveal the interfacial microstructure (interphase) of fibre and matrix, a thin section was extracted at the fibre/matrix region from 350-2 and 400-2 specimens by using focused ion beam (FIB) milling, before imaging using a high-resolution transmission electron microscope (HRTEM, JEM-2100F, JEOL). For evaluating the crystallinity, both differential scanning calorimetry (DSC, Polyma 214, Netzsch) and X-ray diffraction (XRD, X'Pert, PANalytical) were conducted. In DSC, samples weighing approximately 7 mg were extracted from the manufactured composites and encapsulated in aluminium pans, before heating with a temperature ramp of 10 °C/min from ambient temperature to 400 °C under a nitrogen flow. The melting enthalpy ΔH_m and the cold crystallisation enthalpy ΔH_c were used to calculate the crystallinity (X) of the manufactured composites from Ref. [8]:

$$X = \frac{\Delta H_m - \Delta H_c}{(1 - w_f) \times \Delta H_m^{100\%}} \tag{2}$$

where w_f is the weight fraction of fibre and $\Delta H_m^{100\%}$ is the melting enthalpy of an ideal crystal of PEEK (130 J/g). The virgin crystallinity of the tape was also obtained from Equation (2). The crystallinity due to cold crystallisation (X_c) was calculated when analysing the final crystallinity by using [8]:

$$X_c = \frac{\Delta H_c}{(1 - w_f) \times \Delta H_m^{100\%}} \tag{3}$$

XRD was performed on the polished cross-section of composite specimens. The diffraction angular 2θ was varied between 10° and 33°. The crystallinity (X) of the manufactured composites was calculated from:

$$X = \frac{I_c}{I_c + I_a} \tag{4}$$

where I_c is the integral of diffraction intensity of crystalline peaks and I_a

is the integral of diffraction intensity of non-crystalline peaks.

2.3. Residual stress measurement

The residual stresses were measured through the central hole drilling method [18], on one side of the composite ring. As suggested by ASTM E837-20 [22], a strain gauge rosette consisting of three strain gauges with 0°, 45°and 90° directions, were employed for measuring the strain release after hole drilling, as shown in Fig. 3a. Prior to drilling, the strain gauge rosette was attached to the side surface of the specimen through adhesives where the rosette centre was placed at the middle of the specimen and its strain gauge at 0° was positioned in parallel with fibre direction (Fig. 3b). A drill bit with diameter of 1.5 mm was used to drill the hole to reach a final depth of 2 mm, as shown in Fig. 3c. The released strain was directly recorded by the data logger. The calculation of residual stress is based on the released strain and the calibration coefficient [18,23,24]:

$$\begin{Bmatrix} \sigma_0 \\ \sigma_{45} \\ \sigma_{90} \end{Bmatrix} = \begin{bmatrix} C_{11} & C_{12} & C_{13} \\ C_{21} & C_{22} & C_{23} \\ C_{31} & C_{32} & C_{33} \end{bmatrix} \times \begin{Bmatrix} \varepsilon_0 \\ \varepsilon_{45} \\ \varepsilon_{90} \end{Bmatrix} \tag{5}$$

where ε_0, ε_{45}, and ε_{90} are the strains released along different directions that is measured by the hole drilling method, C_{ij} are calibration coefficients, which depend on the material's elastic moduli. As there is no standard approach to obtain calibration coefficients, a finite element (FE) model is usually adopted and has been validated by different researchers [18,24], which was also employed in the present study. More details of the FE model and the calibration matrix used are shown in the Supplementary Material S1.

2.4. Finite element model of ATP process

Fig. 4 shows a snapshot of the 2D finite element model developed for the LATP used. A graded mesh represented the mandrel and roller where the mesh becomes finer when traversing from the centre to the circumference in order to balance computational cost against precision, as shown in Fig. 4a and b. A fine mesh with an element size of 0.056 mm along the thickness direction and 0.5 mm along the length direction (fibre direction) was used for the composite tape (Fig. 4c). A local coordinate was assigned to the tape considering its orthotropic behaviour, where the length direction, i.e., fibre direction is defined as the *x*-direction and the thickness direction is the *z*-direction, as depicted in Fig. 4c. Four-noded thermally coupled quadrilateral elements (CPE4RT) were assigned to the tape mesh. The mandrel was simplified to behave as a rigid body, and the roller was considered to behave elastically. The relevant properties of the roller are shown in Table S2 (See Supplementary Material S2), as obtained from data sheets [25]. The material properties of the steel mandrel, including Young's modulus, Poisson's ratio, thermal expansion coefficient, density, specific heat and heat conductivity were taken from Ref. [26]. The geometry in the model replicates that utilised in the experiment (see Section 2.1). To better address temperature history as well as the residual stress development

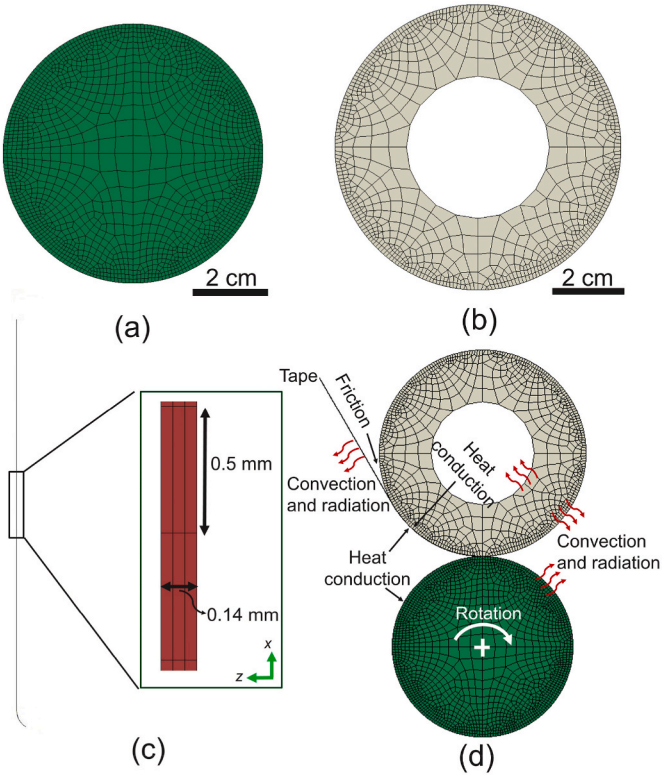

Fig. 4. Illustration of (a) mandrel, (b) roller, (c) tape (showing *x*-direction (fibre), and *z*-direction (width) and (d) assembly including mechanical and thermal boundary conditions used in the model. [The gridlines in all the images represent element boundaries.].

during manufacture, a thermo-optical model to describe the heat flux distribution and a homogenised viscoelastic material model for the composite tape were developed separately. These two models were implemented as subroutines into the FE model using Abaqus, which are detailed next.

2.4.1. Thermo-optical model

A ray-tracing method [11] is used to underpin the thermo-optical model because it can directly visualise the distribution of laser heat flux on the mandrel and tape based on the reflection and absorption behaviour of laser rays. In this method, the laser beam is split into *n* ray, then absorbed and reflected energies of each ray at the location on the substrate and tape were calculated until two reflections were reached. The ray-tracing algorithm is shown in Fig. 5a, which was programmed in MATLAB. The results of one case study are shown in Fig. 5b and c respectively where the laser-material interaction and distribution of heat flux could be extracted. The resulting heat flux distribution on the tape and substrate is then fitted to polynomial expressions and subsequently implemented as subroutines in Abaqus. The fitted results

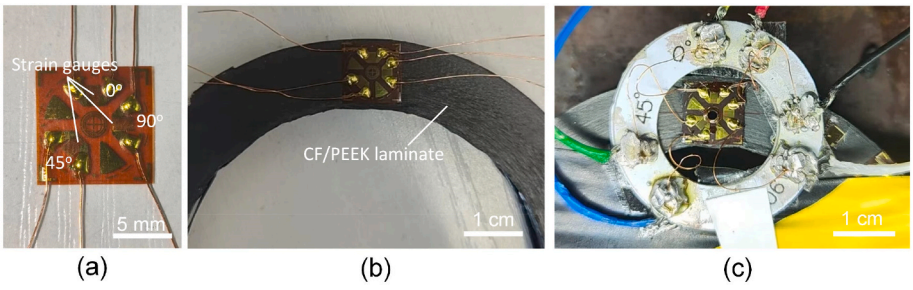

Fig. 3. (a) Strain gauge rosette, (b) strain gauge rosette on the CF/PEEK laminate and (c) after hole drilling.

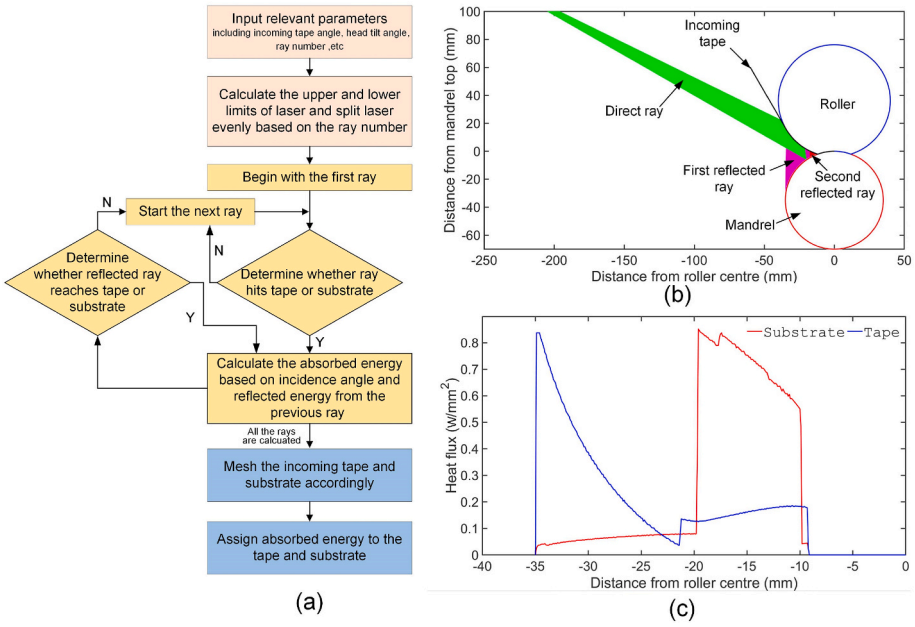

Fig. 5. (a) Algorithm for ray-tracing method, (b) visualised laser-material interactions and (c) distribution of heat flux on substrate and tape.

regarding the heat flux distribution with different parameters are presented in Fig. S2. It should be noted that with an increasing number of deposited layers, the effect of laser on the previously deposited layers becomes increasingly less, so in order to save computational cost, the temperature and stress development of a 4-layer CF/PEEK laminate were simulated in the present study. To validate the developed thermo-optical model, thermocouples with a data acquisition frequency of 6.25 Hz were attached to the mandrel to measure the temperature during manufacture.

2.4.2. Viscoelastic model

It is widely accepted that a viscoelastic model ably predicts the stress of thermoplastic and thermoplastic laminates during manufacturing as polymers demonstrate stress relaxation and creep strains, particularly at high temperatures [27,28]. During LATP, as the processing temperature is often greater than the melting point of the polymer matrix, viscoelastic considerations are necessary. Mao et al. [28] developed a viscoelastic model for thermoplastic matrix composite laminates represented by a number Maxwell elements (N), assembled in parallel, where the stress increment at the reduced time $\xi^{t+\Delta t}$ is:

$$\Delta\sigma_i(\xi^t) = \sum_{w=1}^{N}\left[exp\left(-\frac{\Delta\xi^{t+\Delta t}}{\tau_m}\right)-1\right]\left[S(\xi^{t-\Delta t})\times exp\left(-\frac{\Delta\xi^{t}}{\tau_m}\right)+\frac{\overline{C_{ij}}W_w a_t \Delta\varepsilon_j^t \tau_m}{\Delta t^t}\left(1-exp\left(-\frac{\Delta\xi^{t}}{\tau_m}\right)\right)\right] + C_{ij}^{\infty}\Delta\varepsilon_j^{t+\Delta t} + \sum_{w=1}^{N}\frac{\overline{C_{ij}}W_w a_t \Delta\varepsilon_j^{t+\Delta t}\tau_w}{\Delta t^{t+\Delta t}}\left(1-exp\left(-\frac{\Delta\xi^{t+\Delta t}}{\tau_m}\right)\right) \quad (6)$$

And where C_{ij}^{∞} and C_{ij}^{u} refer to the fully relaxed and unrelaxed stiffness, respectively and $\overline{C_{ij}} = C_{ij}^{u}\text{-}C_{ij}^{\infty}$ is the difference between relaxed and unrelaxed stiffnesses, W_w and τ_m are the weight factor and the relaxation time for the wth Maxwell element, the reduced time $\xi^{t+\Delta t}$ is the sum of ξ^t and $\Delta\xi^{t+\Delta t}$. At a particular time increment, the reduced time increment can be expressed as a function of shift factor (a_t):

$$\Delta\xi^t = \int_{t-\Delta t}^{t}\frac{dt}{a_t} = \frac{\Delta t^t}{a_t} \quad (7)$$

Based on the Time-Temperature superposition principle, the shift factor is a function of temperature and detailed values shift factor for PEEK polymer were taken from Ref. [29].

$S(\xi^{t-\Delta t})$ in Equation (6) is written as:

$$S(\xi^{t-\Delta t}) = \int_0^{\xi^{t-\Delta t}}\overline{C_{ij}}W_w\, exp\left(-\frac{\xi^{t-\Delta t}-\xi'}{\tau_m}\right)\frac{\partial\varepsilon_j}{\partial\xi'}d\xi' \quad (8)$$

The relaxation times (τ_m in equation (6)) for the composite material was considered to be approximately the same as those for the matrix because the viscoelastic behaviour arises from the polymer matrices, as suggested by Refs. [28,30]. The calculation of unrelaxed stiffness of composite laminates was based on classical laminate theory as detailed in Ref. [31], and the detailed values for variables in Equations (6)–(8) used in the present study were obtained from Refs. [11,12,27,29], which are shown in Tables S3–5 in Supplementary Material S3. More descriptions regarding the model are also shown in Supplementary Material S3.

2.4.3. Boundary condition

In the FE model, apart from imposing the upper surface of the substrate and the bottom surface of the incoming tape to be subjected to laser heating (as discussed in Section 2.4.1), the surfaces in contact with the ambient air temperature were subjected to free convection:

$$\varphi = h_c \times (T\text{-}T_{amb}) \quad (9)$$

where $h_c = 13$ W/m^2/K [11], noting the ambient temperature T_{amb} was set to 25 °C. The effect of radiation was also considered using a surface

emissivity of 0.87 [11]. A rough contact was defined between the incoming tape with substrate (this includes the contact between the mandrel surface with first tape layer and between the consolidated tape with the incoming tape) where no slip occurs once two nodal points in two adjacent parts are in contact with each other. The thermal exchange (thermal contact conductance) between the roller and the incoming tape, substrate and mandrel, were set to 436 $W{\cdot}m^{-2}{\cdot}K^{-1}$ [11] and 1000 $W{\cdot}m^{-2}{\cdot}K^{-1}$ [13], respectively. Levy et al. [6] found that the heat exchange coefficient between composite layers varies depending upon the degree of contact, ranging from 2500 to 20000 $W{\cdot}m^{-2}{\cdot}K^{-1}$ when the degree of contact changed from 0.6 to 1. Considering the time for realising intimate contact is rather short (<1s) in LATP [2], a conductance of 10000 $W{\cdot}m^{-2}{\cdot}K^{-1}$was selected to represent the incoming tape and substrate. The defined boundary conditions are depicted in Fig. 4d, to provide greater clarity.

3. Results

3.1. Macro-appearance

Fig. 6 shows the macro-appearance of the specimens manufactured under different processing parameter conditions. Quite distinct differences are readily observed in these specimens in terms of the geometrical size and structure of layers. Specimens prepared under 4 bar compaction pressure (350-4 and 400-4) are considerably thicker than those made at the lower 2 bar pressure (350-2 and 400-2). A severe wrinkle defect can also be observed in specimens 350-4 and 400-4.

The cross-sectional images of the specimens are shown in Fig. 7, where the significant differences in thickness are evident, ranging from 11.3 mm for 350-2 to 14.4 mm for 350-4. During LATP, transverse shear, inducing lateral squeeze flow of CF/PEEK tape [32], is considered to be non-uniform across the width of the tape, especially when the roller starts to lose contact with the mandrel resulting in less restriction to squeeze the edge material. This explains that a relatively uniform layered structure could be seen for the first several layers (Fig. 7), and the wrinkles start to appear afterward (arrows in Fig. 6). In comparison to a 2-bar pressure, a higher consolidation pressure at 4 bars would enhance the non-uniform distribution of the transverse shear stress, which possibly results in a more severe irregularity in the thickness of the composite tape during processing. Therefore, with the progression of LATP, the accumulation of a locally thicker layer, as depicted in Fig. 7 by white arrows, is expected to be the reason for the formation of a thicker laminate at a higher pressure. Specimen 400-2 exhibits an overall uniform layered structure, emphasising the importance of selecting appropriate processing parameters for producing high-quality laminates. Despite the wrinkles being machined before microstructural observation and ILSS testing, an unbonded region resulting from wrinkles remains present in specimens 350-2, 350-4, and 400-4, indicating a relatively large unbonded area in these specimens. Due to the non-uniform distribution of defects in the laminates (especially evident in 350-2, 350-4 and 400-4), the utility of a quantitative investigation of the void content was not thought to be particularly useful and so was not undertaken. Two representative regions, including the area with relatively large defects (unbonded region for 350-2, 350-4 and 400-4) and the bonded region in these specimens (as marked in Fig. 7), were inspected and are presented in Fig. 8.

Observing Fig. 8, it is evident that voids are the most notable defects in the bonded region. In comparison to 350-2, which exhibits voids both at the interface between plies (inter-ply region) and within the plies (intra-ply region), 350-4 displays fewer voids, with the majority located at the inter-ply region. This reduction is attributed to the elevated pressure at a temperature of 350 °C, fostering enhanced contact and reducing void content, particularly in the inter-ply region. However, a higher pressure under a temperature of 400 °C shows an adverse effect where 400-2 has the lowest void content in the bonded region in comparison with 400-4. This effect could happen because, 400 °C is well above the melting point of PEEK matrices (334–343 °C [33]), and the non-uniform matrix flow induced by high pressure may cause a degree of deconsolidation [7,12]. Such behaviour results in the disruption of ply continuity in the unbonded area of specimens 350-4 and 400-4, as illustrated in Fig. 8b_2 and d_2, contributing to the formation of wrinkles, as previously discussed. This discovery suggests that at a low process temperature, an increased consolidation pressure may be advantageous for reducing void content. However, at high processing temperatures, excessive consolidation pressure raises the likelihood of debonding and the formation of significant wrinkles.

3.2. Crystalline morphology and crystallinity

Fig. 9a and b present the DSC and XRD curves for various specimens. The comparison of calculated crystallinity using these two methods is depicted in Fig. 9d, revealing that the crystallinities calculated by DSC broadly agree with those determined by XRD. Additionally, variations in processing parameters do not exhibit a significant effect on crystallinity levels, as all measured values fall within the range of 30%–35%. Despite efforts to assess local crystallinity differences by testing laminates from different locations, i.e., centre and bottom, similar crystallinity levels, as illustrated in Fig. 9c, are obtained. This consistency is probably attributed to the fast crystallisation behaviour of PEEK, driven by its chemical structure. This topic is discussed in detail in Section 4.1.

The crystalline morphology was subsequently examined, identifying two distinct regions influenced by the interaction with the fibres—resin-

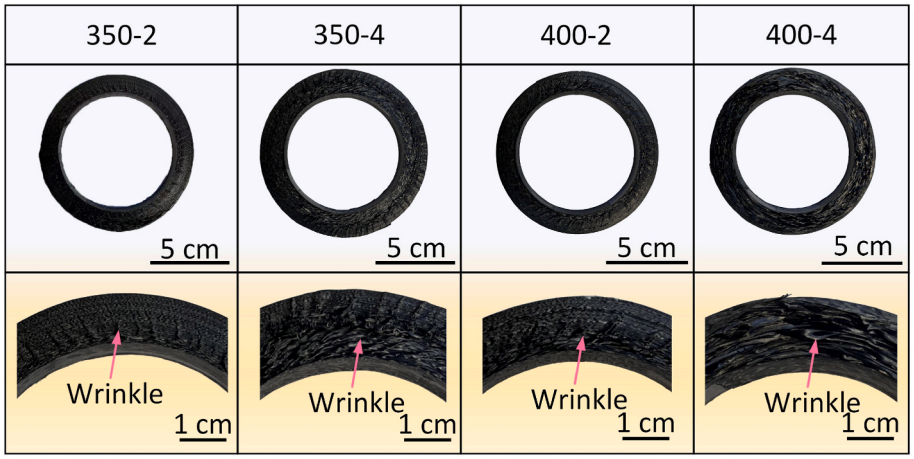

Fig. 6. Macro-appearance of specimens manufactured by different parameters. The second row magnified images show the presence of wrinkles.

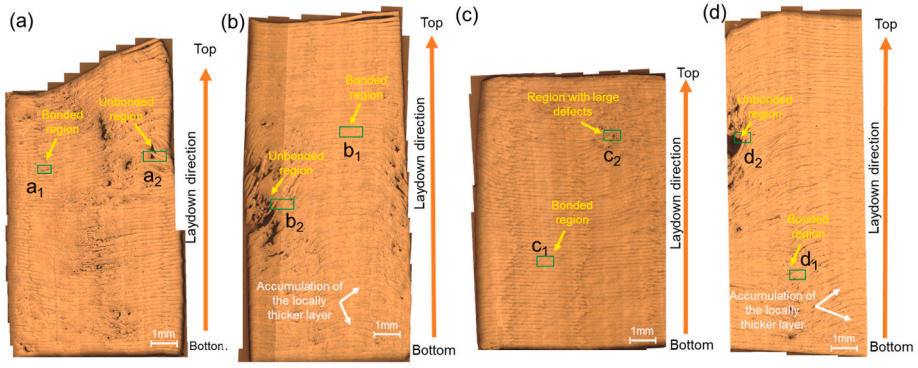

Fig. 7. Cross-sectional images of specimens: (a) 350-2, (b) 350-4, (c) 400-2 and (d) 400-4.

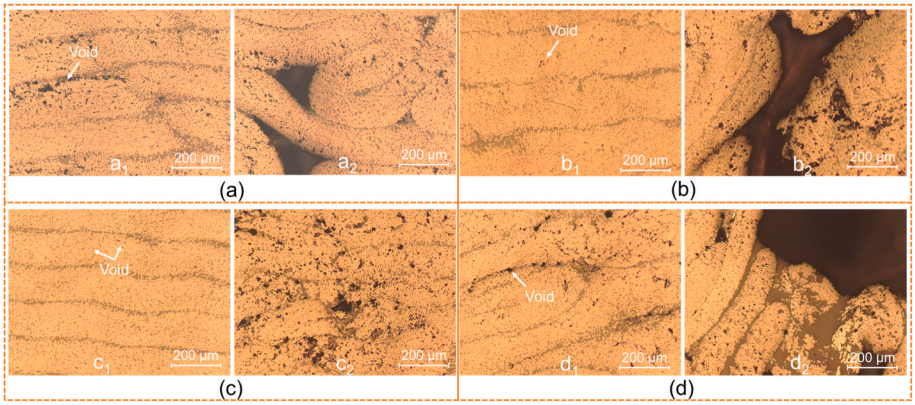

Fig. 8. Magnified optical images: (a) 350-2, (b) 350-4, (c) 400-2 and (d) 400-4 where a_1, b_1, c_1, d_1 indicate the bonded regions and a_2, b_2, c_2, d_2 show the large defect regions.

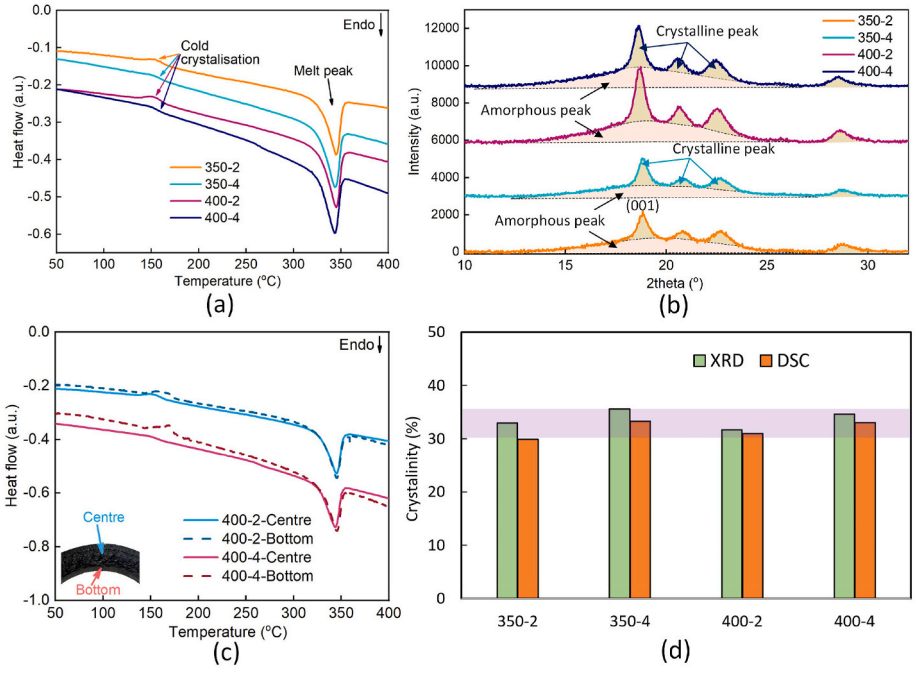

Fig. 9. (a) DSC and (b) XRD curves for different specimens, (c) heat flow curves of 400-2 specimen (bottom inset indicates the locations for acquiring DSC data) and (d) comparison of crystallinity by DSC and XRD (shaded region indicates the crystallinity range) [a.u. in Fig. 8a–c indicates arbitrary unit].

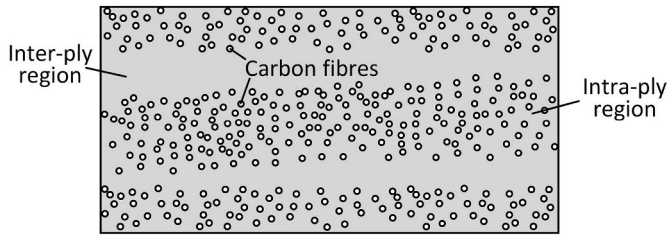

Fig. 10. Cross-sectional illustration of CF/PEEK composite showing the inter- and intra-ply regions (note the illustration is not to scale).

rich regions between the plies (inter-ply region) and those within the plies (intra-ply region), as schematically illustrated in Fig. 10. It is inferred that the matrix in the inter-ply region could be less affected by fibre reinforcements compared to that in the intra-ply region [34].

Fig. 11 depicts the crystalline morphology of CF/PEEK specimens produced under various LATP processing parameters. Amorphous polymer exists in the form of entangled molecular chains, displaying no ordered molecular structures. In semi-crystalline polymers including PEEK, the crystallisation process involves the folding together of polymer chains due to partial alignment, resulting in the formation of ordered molecules. The initial nucleation sites, i.e. nuclei, grow as crystallisation progresses, resulting in larger spherical superstructures, i.e. spherulites, emerging from the arrangement of ordered molecules [35]. In Fig. 11, spherulites are clearly visible in all samples, marked by dashed lines, with nuclei indicated by yellow arrows. The size of spherulites in both inter-ply and intra-ply regions of all specimens is approximately 2–3 μm. Therefore, in the current study, variations in processing parameters show no significant effect on spherulite morphology, consistent with XRD and DSC studies that reveal similar levels of crystallinity (Fig. 11d). Additionally, in the intra-ply region with a high fibre density (Fig. 11a–c, e, and g), almost all nuclei exist in the matrix region between fibres rather than on the fibres themselves. This observation suggests that, in LATP-produced CF/PEEK laminates, the matrix remains a preferable location for homogeneous-like crystallisation processes to occur compared to heterogeneous-like crystallisation processes which would occur at fibre surfaces. Thus, as long as the distance between fibres exceeds 2–3 μm, the presence of fibres has minimal effect on nucleation and subsequent spherulite growth in LATP under the investigated processing parameters.

3.3. Fracture behaviour

Interlaminar shear strength (ILSS) measurements are depicted in bar charts in Fig. 12, with the test configuration illustrated in the top left inset. It is noteworthy that, despite similar crystallinity levels across all four specimens, significant difference in ILSS values is observed. In the CF/PEEK laminate manufactured at a temperature of 350 °C, increasing the pressure from 2 bar to 4 bar leads to an ILSS increase. However, for samples made at a higher temperature (400 °C), higher compaction pressure results in a reduced ILSS. Therefore, specimen 400-2 exhibits the highest ILSS (78 MPa) in the present case.

To elucidate the nature of failure mechanisms, fractographic analyses of post-mortem cross-sectional specimens were performed. The images of major cracks from ILSS testing are shown in Fig. 13, as identified by the yellow arrows. In specimen 350-2 (Fig. 13a), interlaminar failure in the inter-ply region is the dominant mode of fracture, and the existence of large defects (dark holes in the crack path) is a possible location for crack initiation. While in 350-4, a crack originating from large defects can also be observed in Fig. 13b. Moreover, for 350-4, failure in the bonded region consists of both interlaminar and intralaminar cracks with a path shown propagating from one ply to its neighbour that can also be witnessed in this specific specimen (Fig. 13c). Failure only occurs within the ply (intralaminar failure) in 400-2 in different areas, as demonstrated in Fig. 13d and e, suggesting strong degrees of bonding between layers. In 400-4, the crack induced by the large defect region is again responsible for the major failure of the laminate, which is shown in Fig. 13f.

Fig. 14 shows the fracture surfaces of specimens from ILSS tests. A relatively clean fibre surface is presented in 350-2 with little

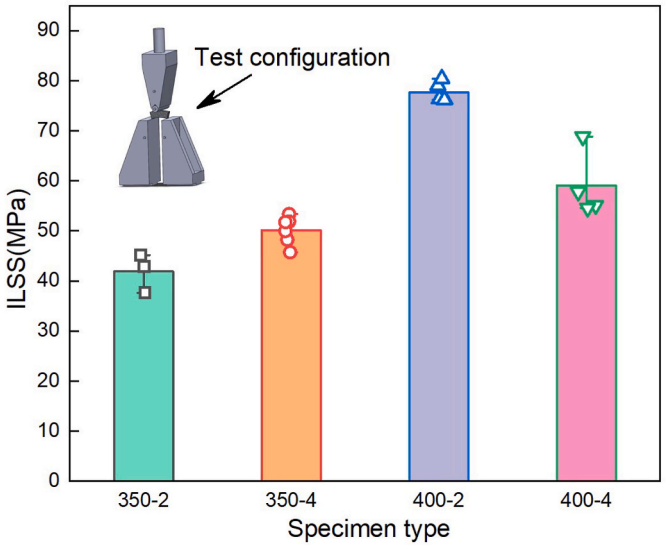

Fig. 12. ILSS results of CF/PEEK laminates. [Tested data points are shown in scatter.].

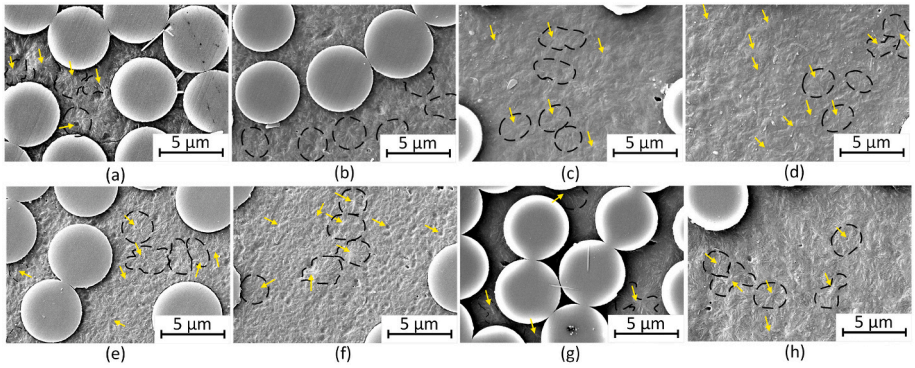

Fig. 11. Crystalline morphology of CF/PEEK laminates at different locations: (a) intra-ply region in 350-2, (b) inter-ply region in 350-2, (c) intra-ply region in 350-4, (d) inter-ply region in 350-4, (e) intra-ply region in 400-2, (f) inter-ply region in 400-2, (g) intra-ply region in 400-4 and (h) inter-ply region in 400-4. [Dashed lines point out the boundary of spherulites.].

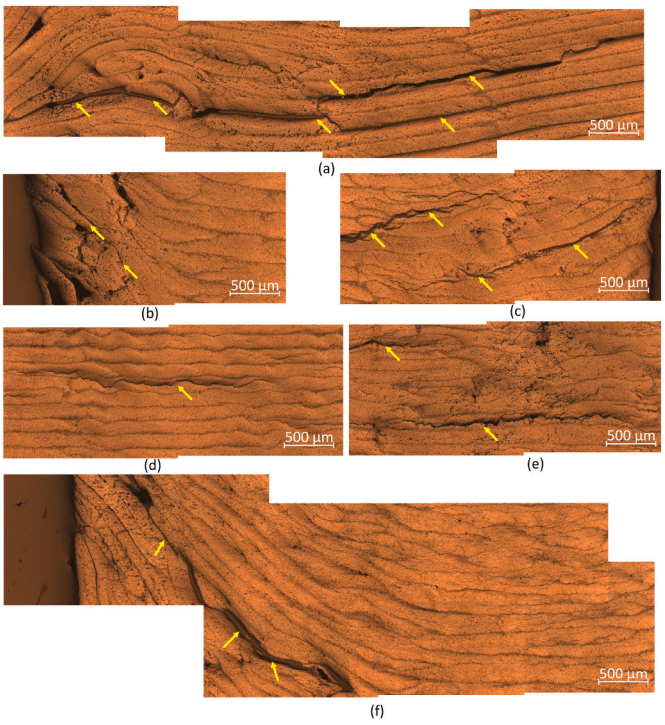

Fig. 13. Fracture path of CF/PEEK laminates from ILSS tests: (a) 350-2, (b) and (c) 350-4, (d) and (e) 400-2 and (f) 400-4. Arrows indicate the crack path.

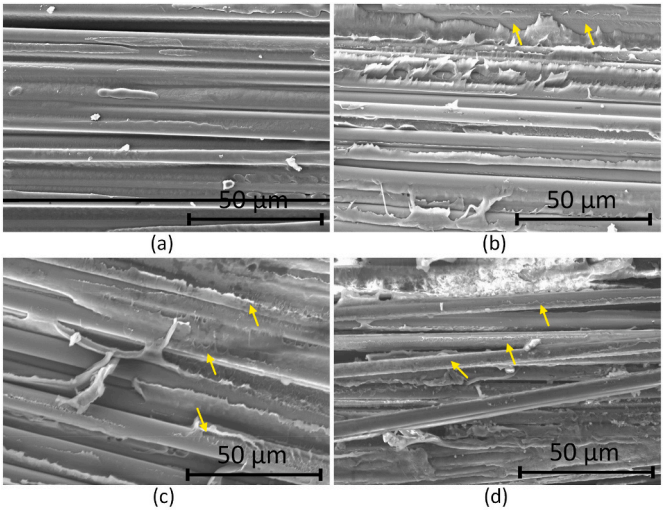

Fig. 14. Fracture surface after ILSS test: (a) 350-2, (b) 350-4, (c) 400-2 and (d) 400-4.[Arrows show matrix remnants on fibres, after failure.].

deformation of the matrix, which is a clear indication of poor degree of bonding between the fibre and the PEEK matrix. The lack of deformation of the matrix is probably due to the existence of a defect in the inter-ply region where tri-axial stress occurs in the event of crack propagation, limiting the deformation of the PEEK polymer [36]. For the 350-4 specimen, although little matrix is attached to the carbon fibre, similar to 350-2, the deformation of PEEK can be observed in Fig. 14b, presumably due to the reduced void volume. In 400-2 and 400-4 specimens (Fig. 14c and d), a significant amount of matrix remains on the fibre surface after fracture, indicating a strong bond between fibre and matrix. Based on these findings, it is noted that in the present case, the ILSS values are largely dependent on the presence of defects and the strength of the fibre/matrix interface because all of the specimens show similar levels of crystallinity. Therefore, numerical simulations were undertaken to further understand the progressive development of microstructure and whether residual stresses have a significant effect on the strength of CF/PEEK laminates.

3.4. Numerical model

3.4.1. Temperature distribution

Fig. 15a and b show the temperature variations with time measured by thermocouples and that by simulation in the cases of 350-2 and 400-2 specimens. The simulated temperature was extracted at the bottom of the first incoming tape (the first layer for the manufactured CF/PEEK). Due to the relatively slow acquisition rate of the thermocouple compared to the extremely higher heating rate of the LATP process, a lower measured peak temperature is obtained. So only the heating and cooling stage obtained by experiments were compared with the simulated results. It is shown that the initial heating stage, as well as the cooling stage from simulation, match reasonably well with the experimental data. Moreover, the processing temperatures, i.e., 350 °C and 400 °C, under two different processing conditions are also well predicted by the simulated peak temperatures (Fig. 15a and b). These observations indicate that the thermo-optical model employed in the present study offers relatively accurate predictions in analysing the temperature development during the LATP process. It should be noted that the first measured peak shows a significantly smaller value in comparison with the simulated data. This difference is due to the fact that the first peak from the measurement just reflects the temperature increment of the thermocouple when subjected to the laser rather than the temperature of the incoming tape because the thermocouple was fixed on the mandrel surface for the measurement. From the temperature profiles shown in Fig. 15a and b, as more tapes are laid down, the cooling time increases even though the peak temperature is lower. Due to the thermal contact conductance between the laser-heated tape and mandrel/roller, there is an increase in the temperature of the mandrel and roller as the LATP proceeds. However, the temperature increase of the mandrel is not significant, which serves as potential reason for the high cooling rate of laminates (see Supplementary Material S5 for more information).

The temperature distribution map on the incoming tape and substrate with different tape layers is displayed in Fig. 15c, in which some characteristic regions, including the highest temperature regions on the incoming tape and substrate, and the shadow region are highlighted. The existence of the shadow region clearly results in a temperature decrease from the highest temperature region to the nip point. The temperature of the incoming tape at different times has similar distributions as shown in Fig. 15c. Interestingly, a slightly different scenario is witnessed regarding the peak temperature value on the substrate. As shown in Fig. 15c, at 3.5 s, with the first layer laying down on the mandrel, the highest temperature on the substrate is greater than that in a similar location after more layers are deposited (for example, at 7.0 s and 11 s where two and three layers were laid down in Fig. 15c). This difference could be explained by the different heat conductances between tape-mandrel and tape-tape, as defined in Section 2.4.3.

Fig. 16a and b show the temperature contour at 8.9 s when two layers were deposited in specimens 350-2 and 350-4. The coordinates were also superimposed in both diagrams, with the top centre of the mandrel set as the origin. The temperature distributions along the bottom of the incoming tape are depicted in Fig. 16c. With an increase in roller pressure from 2 bar to 4 bar, the region showing the highest temperature appears to shift from 10 mm ahead of the centre of the roller to 13 mm. Due to the existence of the shadow area, a gradual temperature decrease is readily observed prior to nip point. Moreover, a more notable drop in temperature happens at the nip point, as depicted by the arrows in Fig. 16c, arising from contact between the hot incoming tape and the substrate. The temperature at the nip point and the temperature decreases in the shadow area (from the region with highest temperature to the nip point, as marked in Fig. 16c) are both shown in Fig. 16d. It is

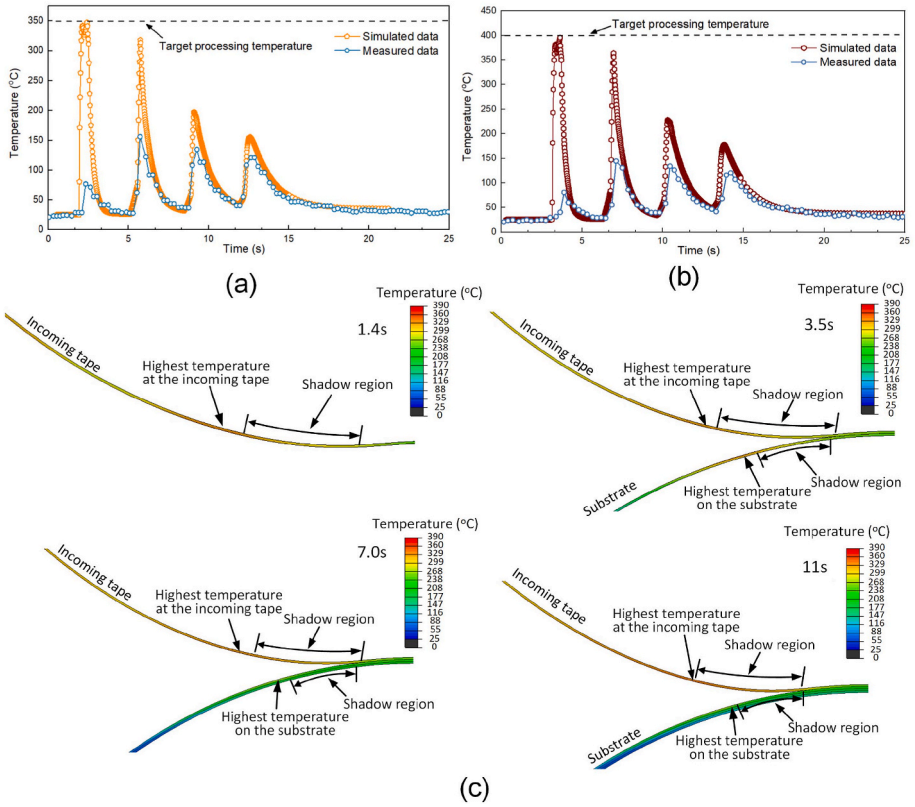

Fig. 15. Comparison between experimentally measured temperature and simulated temperature for (a) 350-2 and (b) 400-2 specimens, and (c) simulated temperature distribution on the incoming tape and substrate at various times for the 350-2 specimen.

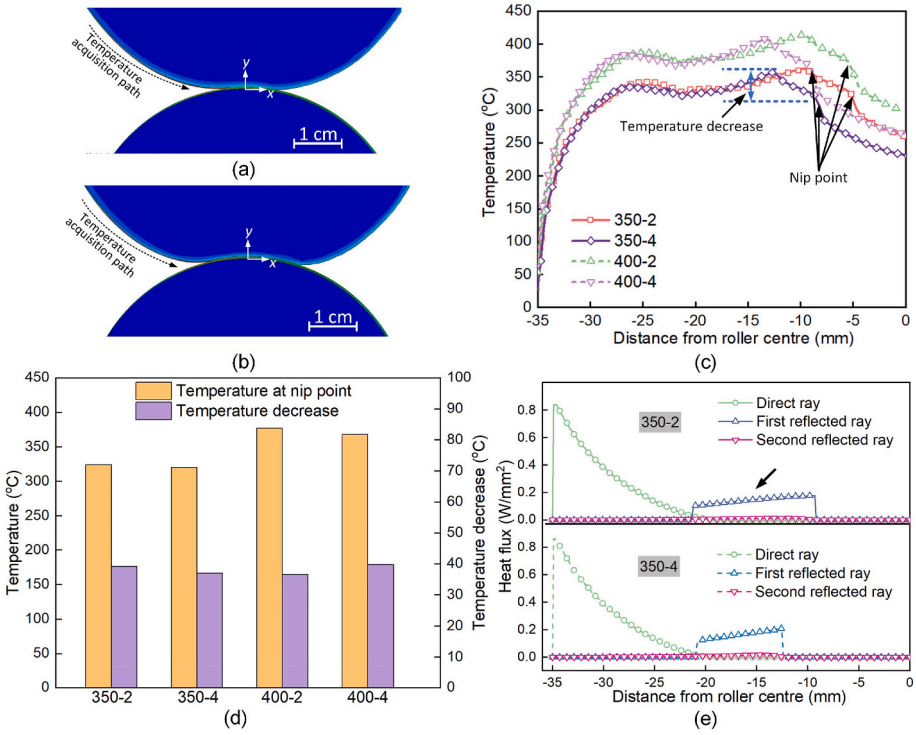

Fig. 16. Snapshot of FE model at 8.9s (2 layers deposited) during LATP manufacturing of (a) 350-2, (b) 350-4, (c) temperature in the bottom region of the incoming tape, (d) temperature at nip point and temperature decrease in the shadow area and (e) distribution of heat flux (arrow shows the heat flux induced by the first reflected ray).

further confirmed that compared to 2 bar pressure, a higher pressure of 4 bar does not lead to a higher nip point temperature nor to a lower temperature decrease. This observation could indicate that increasing the pressure from 2 bar to 4 bar is not necessarily an effective approach to reduce the temperature decrease within the shadow region, even though the length of shadow region is shortened by 0.5 mm due to the deformation of the roller (Fig. 16c). This phenomenon could be explained by the heat flux distribution behaviour, as shown in Fig. 16e. The heat flux generated by the direct ray shows a similar pattern under different pressures, which correspond well with the similar temperature distribution on the incoming tape (at the distance from ~-35 mm to ~ -20 mm in Fig. 16c) arising from the direct laser radiation. But due to different amounts of deformation of the roller under the different pressures (Fig. 16a and b), the heat flux by the first reflected ray is much higher and occurs over a greater distance at a pressure of 2 bar than that at 4 bar, as depicted by the arrow in the top image in Fig. 16e. This response serves as the main cause for the low temperature drop within the shadow region at a lower pressure.

3.4.2. Stress development

The bottom node of the second layer (middle layer of the FE model) was selected to analyse the development of residual stress during LATP, as shown in Fig. 17a. Fig. 17b and c demonstrate the corresponding stress along the fibre direction (σ_x) and thickness direction (σ_z). To better understand the residual stress evolution, the temperature profile was also extracted and superimposed in Fig. 17b and c. Regarding σ_x, the three as-presented cooling processes (from simulation) lead to the residual stress changing from compression to tension due to the rapid change of temperature under the different LATP processing parameters. But the change in sign of residual stress becomes less significant with the continuous deposition of the new layer, indicating that with LATP proceeding, the stress in the bottom layer does not experience notable changes. Interestingly, the change in processing temperature and pressure in the currently investigated range show an insignificant effect on the stress evolution behaviour. A similar trend is also observed for σ_z, where the residual stress change is considerably smaller in the thickness direction. Moreover, the cooling process may not always give tensile residual stresses, but remain in compression after cooling (Fig. 17c). This behaviour is presumably due to the stress relaxation of PEEK polymer during LATP. The total average stress of the second layer with four nodes was calculated and used to compare with the calculated residual stress, with results and corresponding error bars presented in Fig. 17d. It could be argued that the residual stress after cooling is not the final residual stress that develops, but in the current model, the only mechanical boundary condition that is imposed on the tape and substrate is the tape-substrate contact (see Section 2.4), so it is considered that there is no obvious difference in terms of the final stress in comparison to the situation where the substrate moves and a fixed boundary is imposed on the bottom of the laminate, which is a previously used approach for calculating stress [37]. From Fig. 17d, the simulated data shows a relatively good match with the experimentally measured values under the different processing conditions, demonstrating the applicability of the viscoelastic model for analysing the mechanical behaviour of CF/PEEK laminates in LATP. Both the measured and simulated data suggest that the residual stress in two different directions is not greatly affected by the processing parameters used in the study, especially for the stress through the thickness. This analysis suggests that residual stress (at least in the present study) is not the main reason for the large differences in ILSS values observed. But some discrepancies between the experimental and simulated residual stress are still present, which may be caused by different effects: (1) the neglect of crystallisation and gas evolution in the simulation. The present model does not analyse potential other contributions to residual stress, such as property differences (density, specific heat, coefficient of thermal expansion) between crystalline and non-crystalline regions, and the gas evolution leading to the formation of voids [2]. These two factors could lead to relatively minor contributions to residual stress during LATP; (2) the number of layers used in the model. In the current study, the manufacturing process of a four-layer composite was simulated, while in the experiment, a much thicker composite was made (refer to Sections 2.1 and 2.4). As LATP progresses, the newly laid-down layer is assumed to create stress relaxation effects in the deposited layer due to the extended thermal annealing effect, as also reported by Sonmez et al. [16]. These considerations could explain the overpredicted residual stress in the fibre

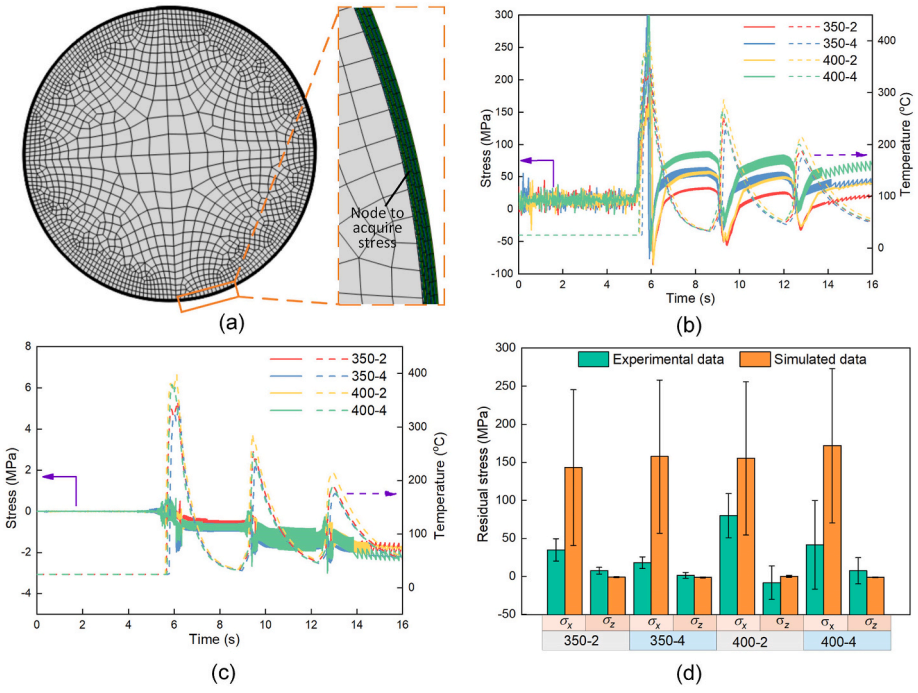

Fig. 17. (a) Illustration of area for the stress analysis, (b) σ_x (fibre direction) and temperature at different times, (c) σ_z (thickness direction) and temperature at different times, (d) comparison of measured residual stress and predicted stress. [Arrows in b and c depict the corresponding axis for the data.].

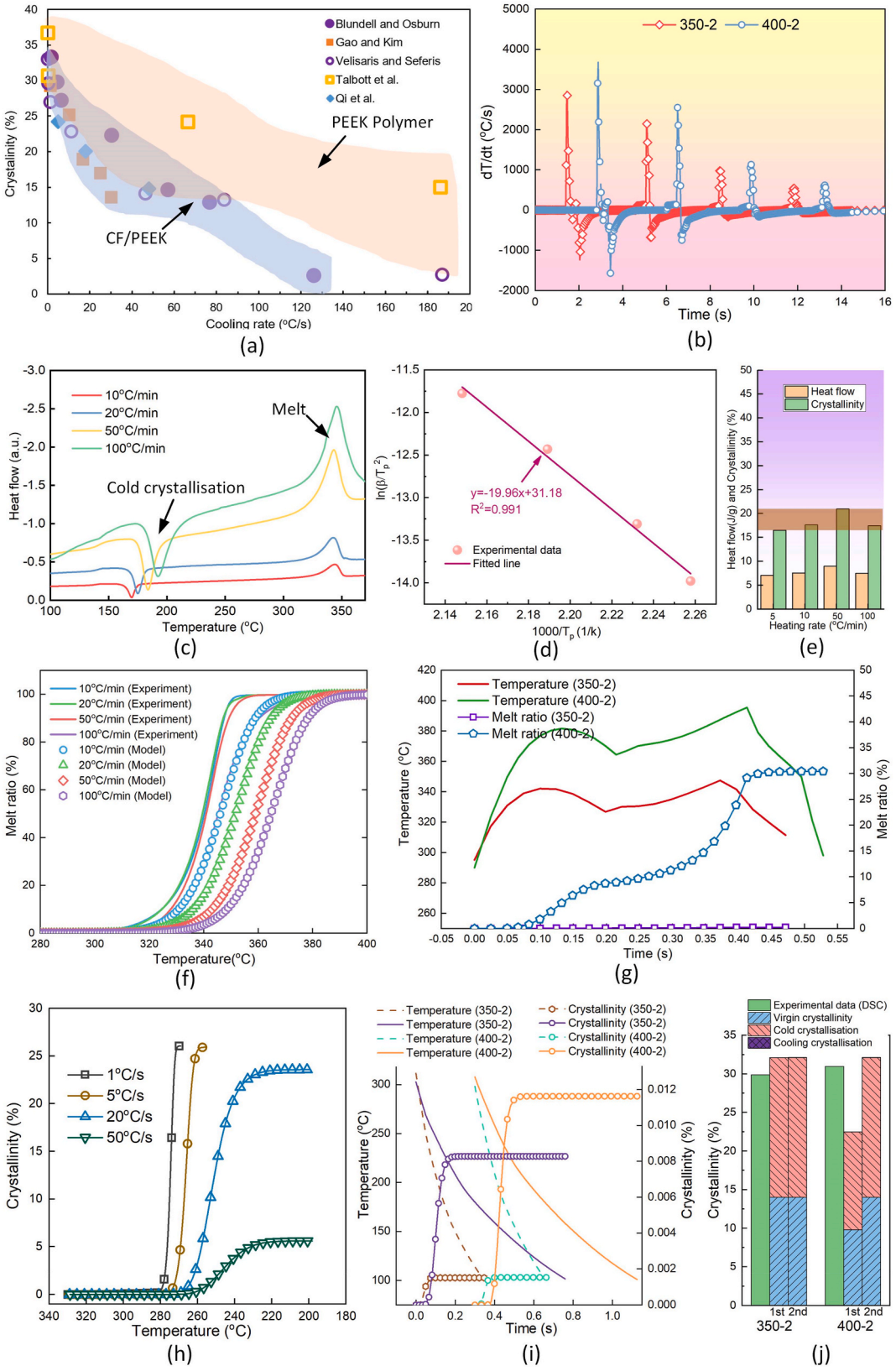

Fig. 18. (a) Crystallinity of PEEK polymer and CF/PEEK under different cooling rates [2,38–41], (b) temperature variation rate of specimens 350-2 and 400-2, (c) heat flow curve of CF/PEEK tape under different heating rates (a.u. indicates arbitrary unit), (d) curve fit from Kissinger's equation, (e) heat flow and crystallinity by cold crystallisation (shaded region indicates the crystallinity range), (f) comparison of fitted melt kinetics model with experimental results, (g) calculated melt ratio under different process parameters, (h) calculated crystallinity under different cooling rates, (i) calculated crystallinity under different process parameters (dashed line indicates the first cooling while solid line shows the second cooling), and (j) comparison of measured and calculated crystallinities (1st and 2nd indicate the first and second heating and cooling cycle).

direction (Fig. 17d); (3) the accuracy of the relevant data in the viscoelastic model. Most of the model data used in the present study were obtained from the literature (see Supplementary Material S4), and slight variations in the viscoelastic behaviour of different PEEK polymers are anticipated. These differences contribute to the discrepancies between simulated and experimental values. Consequently, the development of a more accurate viscoelastic model remains necessary for LATP.

4. Discussion

4.1. Crystallisation behaviour

It has long been noted that processing parameters pose a significant influence on final crystallinity levels, with the cooling rate identified as one of the most crucial factors in determining the crystallinity of PEEK and CF/PEEK. Fig. 18a shows the comparison of crystallinity of PEEK and PEEK/CF with different cooling rates from the melt state [2,38–41], where it is shown that a high cooling rate leads to lower crystallinity. Given the absence of a significant difference in crystallinity at various locations in the LATP-manufactured samples, the temperature history of the bottom tape in 350-2 and 400-2 (Fig. 15a and b) underpins the current discussion. The first derivative of temperature history, representing the heating and cooling rate, was calculated and is depicted in Fig. 18b. Simulated results indicate a cooling rate as high as 1000–3000 °C/s, suggesting a low degree of crystallisation during LATP from melt. Further analysis is therefore required to understand the reasons for the similar crystallinity of specimens manufactured under various parameters in the present case.

The final crystallinity of PEEK/CF is primarily influenced by cold crystallisation, melting upon heating, and subsequent crystallisation during cooling (cooling crystallisation), which is now discussed in detail. In terms of cold crystallisation, a set of dynamic DSC scans was devised, applying different heating rates to the original tape. The results, as shown in Fig. 18c, clearly indicate the occurrence of cold recrystallisation within a temperature range of 150–200 °C. Kissinger's equation derived from the Ozawa model was considered to be a simple and accurate approach to analyse the cold crystallisation process, as demonstrated by Ref. [42]:

$$\frac{\mathrm{d}\left(ln\left(\frac{\beta}{T_P^2}\right)\right)}{\mathrm{d}\left(\frac{1}{T_P}\right)} = -\frac{E_a}{R} \tag{10}$$

where R is the gas constant, β is the heating rate, E_a is the activation energy, T_p is the peak cold crystallisation temperature of the DSC curve. The fitting of Kissinger's equation to the DSC data is displayed in Fig. 18d. The negative slope of the curve fit suggests that cold crystallisation shifts to higher temperatures with an increase in heating rate, consistent with the observations shown in Fig. 18c. The fitted curve indicates that a heating rate of 1000–3000 °C/s (similar to the heating rate in ATP process, Fig. 18b) results in a peak temperature within the range of 258~284 °C. This effect suggests that a complete cold crystallisation may be achieved under all studied processing parameters (the tape can reach temperatures of 350 and 400 °C in the present case), especially considering the subsequent heating process's contribution to the ongoing cold crystallisation process. Additionally, it is observed that the total heat generated during cold crystallisation remains relatively unchanged across different heating rates, as summarised in Fig. 18e. So, the calculated increase in crystallinity due to full cold crystallisation is presented in Fig. 18e and is approximately 18%.

In terms of melting, Maffezzoli et al. [43] developed a melt kinetic model shown to calculate the melt ratio, i.e., the ratio of melt material to total material, X_f:

$$\frac{dX_f}{dt} = -k_0\, exp\left(-\frac{E_a}{RT}\right)\left(1\text{-}X_f\right)^n \tag{11}$$

where k_0 is a coefficient, n is the kinetic order, T is the temperature and E_a is the activation energy of the melting process, and R is the universal gas constant. The relevant values for CF/PEEK are taken from Ref. [43]. The experimentally derived melt behaviour from DSC (Fig. 18c) is compared to the model data in Fig. 18f, revealing an acceptable fit. This melt model is then employed to predict the degree of melt in CF/PEEK laminates during LATP, as depicted in Fig. 18g. The corresponding temperature profile is superimposed, utilising only temperatures above 300 °C in the first heating process for the calculation, as the subsequent pass exhibits a considerably reduced peak temperature (Fig. 15a and b). The results indicate that with an increase in the processing temperature, the degree of melt also rises. However, even at the highest processing temperature (400 °C) used in the present study, only approximately 35% of crystalline PEEK undergoes melting. In contrast, for the 350-2 specimen, the amount of melt is significantly lower, approaching zero.

The crystallisation models of CF/PEEK have also been widely discussed, among which the model proposed by Velisaris and Seferis [40] considered both primary and secondary crystallisation mechanisms, showing excellent match with experimental data. The expression for the crystallinity (X_{cc}) developed is given by:

$$X_{cc} = X_{c\infty} \times \left(w_1 \times F_{vc1} + (1\text{-}w_1) \times F_{vc2}\right) \tag{12}$$

where $X_{c\infty}$ is the equilibrium crystallinity of PEEK, w_1 is the weight factor for the first crystallisation mechanism, F_{vc1} and F_{vc2} are the normalised volume fraction crystallinity for the first and second crystallisations process. More description and detailed values regarding the model can be found in Ref. [40]. The calculated crystallinity of CF/PEEK from melt under different cooling rates is illustrated in Fig. 18h, confirming that the final crystallinity significantly decreases with an increase in cooling rate. For LATP in the present study, the first and second cooling profiles in specimens 350-2 and 400-2 were utilised to calculate the crystallinity resulting from cooling since only the first two temperature cycles lie well within the crystallisation temperature range (from melt temperature to T_g) in LATP (see Fig. 15a and b). The calculated crystallinity during cooling is presented in Fig. 18i, indicating that the total increase in crystallinity from cooling in these two cases (350-2 and 400-2) is rather low, with the highest value reaching only ~0.012%. These results clearly demonstrate that crystallisation upon cooling does not play a significant role in affecting the final crystallinity in the current investigation.

It is important to note that the model assumes complete melting of the crystalline polymer before the occurrence of crystallisation. However, in the present case, due to the high heating rate and short soak time, the polymer matrices do not fully melt, as shown in Fig. 18g, introducing potential errors into the current calculation. Okazaki and Wunderlich [3] reported that a local equilibrium of a small fraction of a partially melted, semi-crystalline, polyethylene terephthalate could recrystallise during the cooling cycle without the need for molecular nucleation. By studying the crystallisation behaviour of PEEK polymer, Tan et al. [44] found that the metastable PEEK melt could also recrystallise immediately among the existing unmelt crystals, but such crystallisation still followed the Avrami phase transformation equation with a fast crystallisation rate. In the meantime, a cold crystallisation was observed in partially melted semi-crystalline poly(3-hydroxybutyrate) [45]. This result indicates that cold crystallisation mainly arises from the uncrystallised partial melt upon cooling. From our results, a similar cold crystallisation scenario was observed for the samples after manufacturing when subjected to DSC analysis (Fig. 9a). Therefore, we conclude that both cold crystallisation and fast crystallisation are potential reasons for the recrystallisation of the partial melt in the cases of 400-2 and 400-4. Due to the lack of relevant data, the calculated crystallinity from cooling shown in Fig. 18i is still used, but the fast

crystallisation during cooling is also included in the following discussion.

The crystallinity after each heating and cooling cycle can be discussed as follows (in the present case, only the first two cycles were used to analyse the crystallisation process):

(i) The crystallinity caused by the first heating and cooling cycle can be readily considered as $X_{f1}=(X_{c1}+X_v) \times (1-X_f) + X_c$, where X_v is the virgin crystallinity from the tape (~14%), X_{c1} is crystallinity increase from cold crystallisation, X_f is the ratio of melt and X_c is the gain in crystallinity from cooling;

(ii) For the second heating and cooling cycle, it is assumed that fast crystallisation from the melted PEEK in the first and second cooling and the appearance of second cold crystallisation recover the virgin crystallinity level from the tape (~14%) and the full crystallinity from cold crystallisation (~18%). The melt and the subsequent crystallisation in the second heating and cooling process are neglected due to their relatively low peak temperature and fast cooling rate.

Based on the above discussion, the comparison of crystallinity in the first and second heating and cooling processes together with the measured crystallinity from LATP samples is shown in Fig. 18j. For 350-2, due to the low degree of melt, the difference of crystallinity after the first and second cycles is relatively insignificant, showing a relatively good match with the experimental results. In terms of 400-2, a relatively high degree of melt (35%) and a low level of cooling crystallisation (~0.012%) result in a drop in crystallinity after the first cycle compared to that in specimen 350-2. Nevertheless, the second heating and cooling cycle leads to a further increase in crystallinity, resulting in a higher final crystallinity than measured (Fig. 18j). Such overprediction is presumably due to the simplification of the crystallisation process occurring in the subsequent cooling and heating process, as just described. However, from the current study, it can be deduced that, depending on the melt ratio of PEEK, crystallisation from cooling may or may not affect the final crystallinity. In contrast, cold crystallisation is considered a significant crystallisation mechanism for CF/PEEK in the present study. So, from the perspective of material selection for LATP, a material showing a strong tendency for cold crystallisation will be beneficial for controlling the total final crystallinity of the composite to meet relevant property requirements.

4.2. Process parameter-microstructure-property relationship

From the ILSS test, it is evident that changes in processing parameters have a significant effect of ILSS results. However, as discussed in Sections 3.4 and 4.1, no significant changes are observed in levels of crystallinity or residual stress. Therefore, the presence of defects and fibre/matrix interfacial properties possibly cause the ILSS variation. As the defects (voids) in CF/PEEK laminates has been discussed previously (see Section 3.1 Macro-appearance), the fibre/matrix interfacial microstructure is now discussed to further analyse the processing parameter-microstructure-mechanical property relationship.

Fig. 19a shows the transmission electron microscope (TEM) sample preparation procedure using the focused ion beam (FIB) technique, during which the fibre/matrix region was located and extracted. The TEM image of the fibre/matrix interface of the 350-2 specimen is presented in Fig. 19b, where a distinct (incoherent) interface between the fibre and matrix is readily observed. The higher magnification in Fig. 19c further confirms that there is no obvious transitional region (interphase) in the fibre/matrix region. The well-aligned crystalline structure can be observed on the fibre side, as presented in the top image

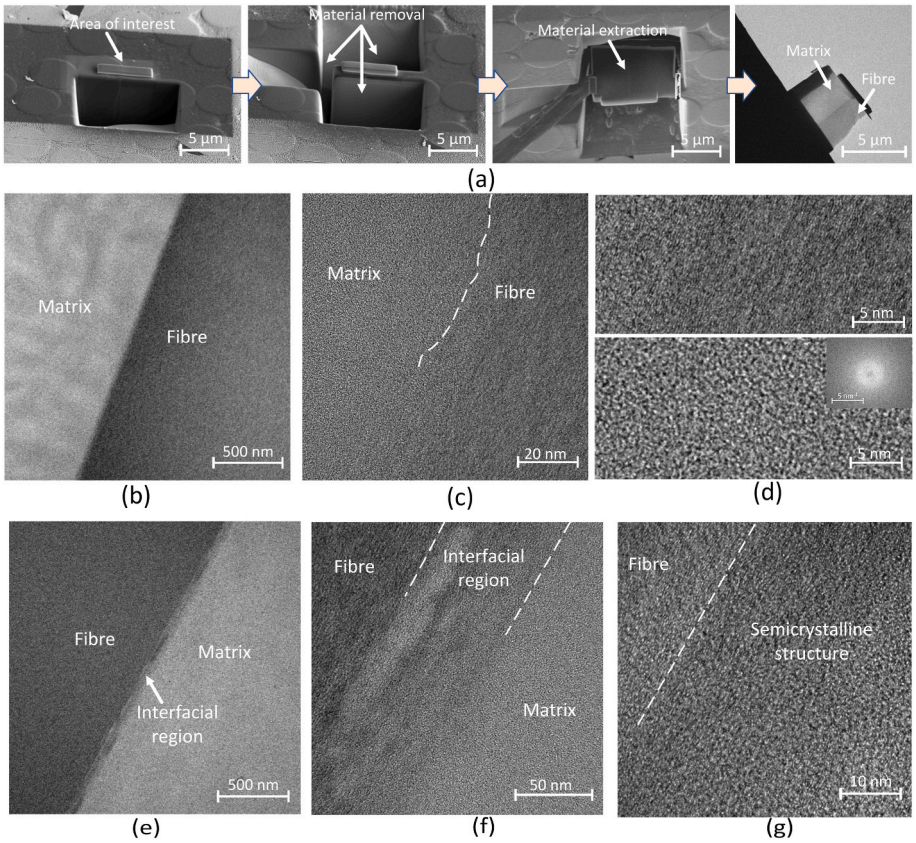

Fig. 19. (a) Preparation of TEM samples by FIB, (b) fire-matrix interface of 350-2, (c) magnified fibre/matrix interface of 350-2, (d) HRTEM of fibre (top) and matrix (bottom, top left inset shows the corresponding FFT pattern), (e) fibre/matrix interface (interphase) of 400-2, (f) magnified fibre/matrix interface of 400-2, (g) HRTEM of the interphase.

of Fig. 19d. However, the fast Fourier transformation pattern of the matrix region (top left inset of the bottom image in Fig. 19d), close to the interface, implies that the matrix is in an amorphous state, indicating that no crystallisation occurred during LATP in the interface region. This observation corresponds well with the morphological studies in Fig. 11, where the nuclei preferably locate in the matrix region rather than at the fibre surface. In terms of the 400-2 specimen, an interphase is readily observed at the fibre/matrix interface, as displayed in Fig. 19e. The image (Fig. 19f) with higher magnification offers much clearer evidence of the formation of an interphase with an average length (thickness) of ~70 nm. A high-resolution TEM (HRTEM) image further clarifies the formation of a semi-crystalline structure that consists of both crystalline and amorphous phases. It is notable that it appears that the PEEK crystalline phase aligns with the carbon fibre making the interface indistinguishable in the vicinity of the fibre, in effect creating a coherent region of aligned crystalline molecules of both carbon fibre and PEEK. These observations indicate that a higher processing temperature is beneficial for the growth of the interphase, essentially enhancing the load transfer ability from the fibre to the matrix under loading conditions. This is consistent with the fractography (Fig. 14) investigation, where a stronger interfacial bonding was confirmed in the specimen 400-2.

The processing parameter-microstructure-mechanical property relationship is now discussed based on the summary of current findings. In the case of the processing temperature of 350 °C, although the temperature is sufficiently high to enable cold crystallisation during the heating process, when the incoming tape reaches the nip point, the temperature drops to around ~300 °C (Fig. 14d), resulting in a viscous resin matrix. As a result, resin flow is insufficient during contact, leading to incomplete diffusion of polymer chains and the generation of voids in the inter-ply region. However, applying a higher pressure from the roller could enhance material flow to some extent, promoting the disappearance of voids in the inter-ply region, as observed in Fig. 7b. At the same time, the viscous resin could exhibit unstable resin flow behaviour, leading to the formation of a large unbonded region, especially at the edges of both sides of the laminate. This processing temperature (350 °C) is also not conducive to the growth of the fibre/matrix interphase. Therefore, a relatively low interlaminar shear strength could be expected, yet increasing the applied roller pressure could improve the resulting bonding quality. Increasing the processing temperature to 400 °C, on one hand, results in more of the PEEK melting during heating. However, the uncrystallised amorphous material from the first heating and cooling cycle can crystallise during the subsequent process, which maintains the final crystallinity at a relatively high level (~31%). On the other hand, the processing temperature at 400 °C also promotes the rearrangement of the fibre/matrix interfacial microstructure, causing the formation of an interphase at the nanoscale. When the material reaches the nip point, a relatively high temperature is still expected (~350 °C). Such a relatively high temperature is beneficial for molecular diffusion in the inter-ply region under moderate pressure, leading to the elimination of voids. Therefore, a relatively high degree of bonding, together with a similar crystallinity to those processed at lower temperatures (350-2 and 350-4), can be achieved. Nevertheless, upon increasing to a higher roller pressure, unstable material flow could contribute to the reappearance of an unbonded region, causing the formation of significant defects, which lowers the interlaminar shear strength of manufactured samples. Therefore, increasing the processing temperature, while not affecting cold crystallisation, and maintaining stable resin flow are considered key factors for achieving good bond strength in laminates. However, it is noted that voids remain in the intra-ply region in specimen 400-2, so further optimisation of processing temperature and roller pressure, adhering to the lessons learnt herein, would be needed to obtain defect-free composites made by LATP.

5. Conclusion

In this study, the relationship between microstructure and interlaminar shear strength (ILSS) in CF/PEEK laminates manufactured by LATP has been explored, drawing insights from a combination of physical experiments and simulation results. The key findings are outlined below:

1. Raising the nip point temperature from 350 °C to 400 °C effectively reduced void formation between plies and minimised the occurrence of unbonded regions with large defects when applying a compaction roller pressure of 2 bar. Increasing compaction pressure at a low processing temperature (350 °C) was found to be beneficial for suppressing voids, however, at a higher processing temperature (400 °C), a larger unbonded region appeared at a pressure of 4 bar.
2. Despite significant variations in ILSS among specimens processed under different processing conditions, no significant effect on crystallinity or crystalline morphology was observed. Spherulites with sizes ranging from 2 to 3 μm were consistently formed. The specimen processed at a processing temperature of 400 °C with a pressure of 2 bar exhibited the highest ILSS values.
3. Simulation results indicated that higher roller pressures led to a similar temperature decrease in the shadow region. Both experimental and simulation results revealed that residual stress was not significantly affected by changes in processing parameters.
4. The marginal variations in crystallinities across specimens were attributed to the occurrence of cold crystallisation processes and the possible fast crystallisation behaviour of the partially melted PEEK when processed under 400 °C. Employing a processing temperature of 400 °C during LATP facilitated the creation of a semi-crystallised coherent fibre/matrix interphase, approximately 50–70 nm in length (thickness), whilst a distinct incoherent fibre/matrix interface was observed in samples prepared at 350 °C. These morphological differences are postulated to be key factors contributing to the divergent ILSS values observed in laminates in combination with pre-existing defects.

CRediT authorship contribution statement

Hong Ma: Writing – original draft, Visualization, Validation, Software, Methodology, Investigation, Formal analysis, Data curation, Conceptualization. **Aswani Kumar Bandaru:** Writing – review & editing, Visualization, Investigation, Formal analysis, Data curation, Conceptualization. **Paul M. Weaver:** Writing – review & editing, Project administration, Investigation, Funding acquisition, Formal analysis, Data curation, Conceptualization.

Declaration of competing interest

The authors declare that they have no known competing financial interests or personal relationships that could have appeared to influence the work reported in this paper.

Data availability

Data will be made available on request.

Acknowledgements

The authors would like to acknowledge Science Foundation Ireland (SFI) for funding Spatially and Temporally VARIable COMPosite Structures (VARICOMP) Grant No. (15/RP/2773) under its Research Professor programme. The first author would like to thank Mr. Liang from Shandong University for performing the residual stress measurement. All authors would like to thank two anonymous reviewers for their thoughtful and helpful comments which have improved understanding

of our observations.

Appendix A. Supplementary data

Supplementary data to this article can be found online at https://doi.org/10.1016/j.compositesb.2024.111293.

References

[1] Frketic J, Dickens T, Ramakrishnan S. Automated manufacturing and processing of fiber-reinforced polymer (FRP) composites: an additive review of contemporary and modern techniques for advanced materials manufacturing. Addit Manuf 2017;14:69–86.

[2] Donough MJ, St John NA, Philips AW, Gangadhara Prusty B, Shafaq, St John NA. Process modelling of in-situ consolidated thermoplastic composite by automated fibre placement – a review. Composer Part A Appl Sci Manuf 2022;163:107179.

[3] Chanteli A, Bandaru AK, Peeters D, O'Higgins RM, Weaver PM. Influence of repass treatment on carbon fibre-reinforced PEEK composites manufactured using laser-assisted automatic tape placement. Compos Struct 2020;248:112539.

[4] Comer AJ, Ray D, Obande WO, Jones D, Lyons J, Rosca I, O'Higgins RM, McCarthy MA. Mechanical characterisation of carbon fibre-PEEK manufactured by laser-assisted automated-tape-placement and autoclave. Composer Part A Appl Sci Manuf 2015;69:10–20.

[5] Risteska S, Samak S, Samak V. The factors that affect the expansion of the tape for it to avoid side effects in the production of composites in online LATP technology. J. Compos. Sci. 2021;5:284.

[6] Levy A, Heider D, Tierney J, Gillespie JW. Inter-layer thermal contact resistance evolution with the degree of intimate contact in the processing of thermoplastic composite laminates. J Compos Mater 2014;48:491–503.

[7] Shafaq, Donough MJ, Farnsworth AL, Phillips AW, St John NA, Gangadhara Prusty B. Influence of deposition rates on the mode I fracture toughness of in-situ consolidated thermoplastic composites. Compos Part B 2023;251:110474.

[8] Kotzur K, Chadwick AR, Löbbecke M. Moderation of thermoplastic composite crystallinity and mechanical properties through in-situ manufacturing and post-manufacturing tempering: Part 2 – morphological characterisation. Composer Part A Appl Sci Manuf 2022;163:107225.

[9] Lü H, Schlottermüller M, Himmel N, Schledjewski R. Effects of tape tension on residual stress in thermoplastic composite filament winding. J Thermoplast Compos Mater 2005;18:469–87.

[10] Stokes-Griffin CM, Kollmannsberger A, Compston P, Drechsler K. The effect of processing temperature on wedge peel strength of CF/PA 6 laminates manufactured in a laser tape placement process. Composer Part A Appl Sci Manuf 2019;121:84–91.

[11] Baho O, Ausias G, Grohens Y, Férec J. Simulation of laser heating distribution for a thermoplastic composite: effects of AFP head parameters. Int J Adv Manuf Technol 2020;110:2105–17.

[12] Islam F, Donough MJ, Oromiehie E, Phillips AW, St John NA, Prusty BG. Modelling the effect of hot gas torch heating on adjacent tows during automated fibre placement consolidation of thermoplastic composites. J Thermoplast Compos Mater 2022;36:1–26.

[13] Hosseini SMA, Baran I, van Drongelen M, Akkerman R. On the temperature evolution during continuous laser-assisted tape winding of multiple C/PEEK layers: the effect of roller deformation. Int J Material Form 2021;14:203–21.

[14] Stokes-Griffin CM, Compston P, Matuszyk TI, Cardew-Hall MJ. Thermal modelling of the laser-assisted thermoplastic tape placement process. J Thermoplast Compos Mater 2015;28:1445–62.

[15] Baho O, Ausias G, Grohens Y, Barile M, Lecce L, Férec J. Automated fibre placement process for a new hybrid material: a numerical tool for predicting an efficient heating law. Composer Part A Appl Sci Manuf 2021;144:106360.

[16] Sonmez FO, Hahn HT, Akbulut M. Analysis of process-induced residual stresses in tape placement. J Thermoplast Compos Mater 2002;15:525–44.

[17] Heathman N, Koirala P, Yap T, Emami A, Tehrani M. In situ consolidation of carbon fiber PAEK via laser-assisted automated fiber placement. Composites Part B 2023;249:110405.

[18] Ghasemi AR, Taheri-Behrooz F, Shokrieh MM. Measuring residual stresses in composite materials using the simulated hole drilling method. Residual Stresses in Composite Materials. (second ed.). Elsevier Ltd.; 2021.

[19] Martín MI, Rodríguez-Lence F, Güemes A, Fernández-López A, Pérez-Maqueda LA, Perejón A. On the determination of thermal degradation effects and detection techniques for thermoplastic composites obtained by automatic lamination. Composer Part A Appl Sci Manuf 2018;111:23–32.

[20] ASTM D2344. Standard test method for short-beam strength of polymer matrix composite materials and their laminates. ASTM Int.; 2002.

[21] ISO 14130, Fibre-reinforced plastic composites - determination of apparent interlaminar shear strength by short-beam method. Geneva, Switzerland: International Organization for Standardization; 1997.

[22] ASTM E837-20. Standard test method for determining residual stresses by the hole-drilling strain-gage method, vols. 1–16. ASTM Int.; 2013.

[23] Ghasemi AR, Mohammadi MM. Residual stress measurement of fiber metal laminates using incremental hole-drilling technique in consideration of the integral method. Int J Mech Sci 2016;114:246–56.

[24] Wu T, Ma Y, Xia H, Geng P, Niendorf T, Ma N. Measurement and simulation of residual stresses in laser welded CFRP/steel lap joints. Compos Struct 2022;292:115687.

[25] SYLGARD™ 184 silicone elastomer. Tech. Data Sheet 2017:1–4.

[26] Deng D, Murakawa H. Numerical simulation of temperature field and residual stress in multi-pass welds in stainless steel pipe and comparison with experimental measurements. Comput Mater Sci 2006;37:269–77.

[27] Doll N. Modeling thermomechanical behavior of polymer gears. University of Wisconsin-Madison; 2015.

[28] Mao H, Yan H, Guo W, Meng Z, Deng J. A three-dimensional viscoelastic analysis of thermoplastic resin matrix composite laminates during hot stamping. Mater Res Express 2021;8:015306.

[29] Kaka D, Rongong J, Hodzic A, Lord C. Dynamic mechanical properties of carbon nanotube-peek nanocomposite. 16th Eur. Conf. Compos. Mater. ECCM 2014:1–8.

[30] Ma X, Wen L, Xiao J, Wang S, Lei M. Bottom-up analysis framework for the continuous multidirectional carbon fiber-reinforced PEEK composite laminates. Polym Compos 2023;44:9026–48.

[31] White SR, Kim Y. PROCESS-INDUCED residual stress analysis of AS4/3501-6 composite material. Mech Compos Mater Struct 1998;5:153–86.

[32] Deignan A, Stanley WF, Mccarthy MA. Insights into wide variations in carbon fibre/polyetheretherketone rheology data under automated tape placement processing conditions. J Compos Mater 2018;52:2213–28.

[33] Hsiao BS, Chang IY, Sauer BB. Isothermal crystallization kinetics of poly(ether ketone ketone) and its carbon-fibre-reinforced composites. Polymer (Guildf) 1991;32:2799–805.

[34] Ma H, Aravand MA, Falzon BG. Influence on fracture toughness arising from controlled morphology of multiphase toughened epoxy resins in the presence of fibre reinforcement. Compos Sci Technol 2022;217:109095.

[35] Pérez-Martín H, Mackenzie P, Baidak A, Ó Brádaigh CM, Ray D. Crystallinity studies of PEKK and carbon fibre/PEKK composites: a review. Composites Part B 2021;223:109127.

[36] Cogswell F. Thermoplastic aromatic polymer composites: a study of the structure, processing and properties of carbon fibre-reinforced polyetheretherketone and related materials. Butterworth-Heinemann; 1992.

[37] Ding A, Li S, Sun J, Wang J, Zu L. A thermo-viscoelastic model of process-induced residual stresses in composite structures with considering thermal dependence. Compos Struct 2016;136:34–43.

[38] Qi Z, Xu Z, Li F, Yao C. Effect of cooling strategy on the bearing capacity of CF/PEEK composite hole. Composites Part B 2023;250:110406.

[39] Talbott MF, Springer GS, Berglund LA. The effects of crystallinity on the mechanical properties of PEEK polymer and graphite fiber reinforced PEEK. J Compos Mater 1987;21:1056–81.

[40] Velisaris CN, Seferis JC. Crystallization kinetics of polyetheretherketone (peek) matrices. Polym Eng Sci 1986;26:1–23.

[41] Gao SL, Kim JK. Cooling rate influences in carbon fibre/PEEK composites. Part 1. Crystallinity and interface adhesion. Composer Part A Appl Sci Manuf 2000;31:517–30.

[42] Wellen RMR, Canedo EL. On the Kissinger equation and the estimate of activation energies for non-isothermal cold crystallization of PET. Polym Test 2014;40:33–8.

[43] Tierney JJ, Gillespie JW. Crystallization kinetics behavior of PEEK based composites exposed to high heating and cooling rates. Composer Part A Appl Sci Manuf 2004;35:547–58.

[44] Tan S, Su A, Luo J, Zhou E. Crystallization kinetics of poly(ether ether ketone) (PEEK) from its metastable melt. Polymer (Guildf) 1999;40:1223–31.

[45] Wellen RMR, Rabello MS, Araujo IC, Fechine GJM, Canedo EL. Melting and crystallization of poly(3-hydroxybutyrate): effect of heating/cooling rates on phase transformation. Polímeros 2015;25:296–304.